Journal of Power Sources 199 (2012) 207–213

Contents lists available at SciVerse ScienceDirect

Journal of Power Sources

journal homepage: www.elsevier.com/locate/jpowsour

Short communication

Ex situ and *in situ* evaluation of carbon ion-implanted stainless steel bipolar plates in polymer electrolyte membrane fuel cells

Kai Feng[a], Tao Hu[b], Xun Cai[a,*], Zhuguo Li[a,**], Paul K. Chu[b,***]

[a] Shanghai Key Laboratory of Materials Laser Processing and Modification, School of Materials Science and Engineering, Shanghai Jiao Tong University, Shanghai 200240, China
[b] Department of Physics and Materials Science, City University of Hong Kong, Tat Chee Avenue, Kowloon, Hong Kong, China

ARTICLE INFO

Article history:
Received 1 September 2011
Received in revised form
20 September 2011
Accepted 21 September 2011
Available online 4 October 2011

Keywords:
Carbon ion implantation
Bipolar plates
Polymer electrolyte membrane fuel cells
Corrosion resistance
Single cell performance
TEM

ABSTRACT

The desirable properties of metallic bipolar plates in polymer electrolyte membrane fuel cells are good corrosion resistance and high electrical conductance. In this study, carbon-implanted SS316L stainless steel bipolar plates are evaluated by various *ex situ* and *in situ* methods. X-ray photoelectron spectroscopy and transmission electron microscopy reveal a carbon-enriched layer with a thickness of about 240 nm thick. The structure depends on the ion implantation fluence. The interfacial contact resistance and electrochemical behavior are determined using *ex situ* techniques. The interfacial contact resistance decreases with increasing ion implantation fluence. The results obtained by potentiodynamic tests, potentiostatic tests, and inductively coupled plasma optical emission spectrometry measurements are consistent with each other confirming that the corrosion resistance is significantly improved after carbon ion implantation. The carbon-implanted stainless steel bipolar plates are assembled into single cells to undergo *in situ* evaluation. The peak power density of the carbon-implanted bipolar plate increases from 566.5 mW cm^{-2} to 840.0 mW cm^{-2} and the power density at 0.6 V increases by a factor of two compared to those measured from a single cell made of unimplanted stainless steel bipolar plates.

1. Introduction

A key challenge for the commercialization of polymer electrolyte membrane fuel cells (PEMFCs) is the development of low-cost bipolar plates suitable for rapid manufacturing while meeting the stringent performance and durability requirements [1–4]. The bipolar plates constitute over 80% of the total stack weight and considerable proportion of the materials cost in a typical fuel cell stack [5,6]. By 2009, the cost of bipolar plates has been reduced to \$6 kW^{-1}, which accounts for more than 20% fuel cell stack cost and 10% total cost [2]. Three types of materials have been proposed and they are graphite/carbon-based composites, polymer/graphite compounds, and metals [3,7,8]. From the standpoint of cost, manufacturability, mechanical strength, and gas impermeability, thin stamped stainless steel foils are promising [9–11]. Nevertheless, the interfacial contact resistance (ICR) and corrosion resistance must still be improved as these factors affect the performance and durability of PEMFCs. Although stainless steels (SS) possess low bulk electrical resistance, the ICR is unacceptably high on account of its self-passivating nature. Stainless steels are also susceptible to dissolution leading to leaching of metal ions into the PEMFC environment, poisoning of the MEAs, and loss of performance [11,12]. Therefore, various surface modification techniques have been investigated in order to improve the performance of SS bipolar plates [13–17]. For instance, incorporation of some elements capable of enhancing the corrosion resistance and electrical conductance into bipolar plate materials surface is a good technique [18]. In this respect, ion implantation is an excellent surface modification technique since elements that can boost the corrosion resistance and conductivity can be implanted into the materials without thermodynamic limitations pertaining to solubility and phase diagrams [19–23]. Owing to the high electrochemical inertness and good electrical conductivity of carbon [24–27], Nikam et al. [28] have conducted low temperature carburization to improve the corrosion resistance and surface conductivity of SS316L and a carbon concentration as high as 14 at.% can be accomplished by this means. Kim et al. [29] have applied carbon ion implantation to improve the corrosion resistance and contact resistance of Ni-base amorphous alloys. The results indicate that, due to the formation of C and Nb passive layers, the ICR is greatly decreased to the level of graphite while the corrosion resistance of both the carbon implanted and non-implanted amorphous alloy are superior to that of SS316L. In this study, carbon ion implantation is performed to improve the corrosion resistance and surface electrical conductivity of stainless steels, the surface structure of SS316L after

* Corresponding author. Tel.: +86 21 54748940; fax: +86 21 62182903.
** Corresponding author. Tel.: +86 21 54748940; fax: +86 21 34203024.
*** Corresponding author. Tel.: +852 34427724; fax: +852 34420542.
E-mail addresses: xcai@sjtu.edu.cn, fengkai@sjtu.edu.cn (X. Cai), lizg@sjtu.edu.cn (Z. Li), paul.chu@cityu.edu.hk (P.K. Chu).

0378-7753/$ – see front matter.
doi:10.1016/j.jpowsour.2011.09.095

Table 1
Nominal chemical composition of SS316L (at.%).

Cr	Ni	Mo	C	Mn	Si	P	S	Fe
20.0–21.0	6.0–7.0	1.5	0.03	1.5	1.0	0.04	0.03	Balance

carbon ion implantation with different implantation dose is investigated and the performance of the ion-implanted SS bipolar plates are evaluated by various *ex situ* and *in situ* methods.

2. Experimental details

2.1. Ion implantation and characterization of implanted layer

Austenitic 316L stainless steel samples with the nominal chemical composition shown in Table 1 were used in this investigation. The stainless steel plates were cut into 10 mm × 10 mm coupons, mechanically polished by SiC 1200 grade waterproof abrasive paper, cleaned with alcohol ultrasonically, and dried. Carbon ion implantation was conducted on the HEMII-80 high-energy metal ion implanter in the Plasma Laboratory of City University of Hong Kong (Fig. 1). The energetic ions were produced by MEVVA ion source, in which the highly ionized plasmas were produced by cathodic vacuum arcs from graphite electrode. Then, the charged ions formed in the plasma can be extracted and accelerated by the strong electric field between extraction electrodes. The vacuum in the implantation chamber was below 5.0×10^{-5} Pa and the carbon cathode was 99.9% pure. The accelerating voltage was 40 kV and the implantation time was 0.25 h, 0.5 h, 1 h, or 2 h. The ion implantation fluence is calculated according to the following formula:

$$D \ (\text{ions/cm}^2) = k\frac{I_m \cdot \tau \cdot n}{e \cdot S \cdot \bar{n}_0} \quad (1)$$

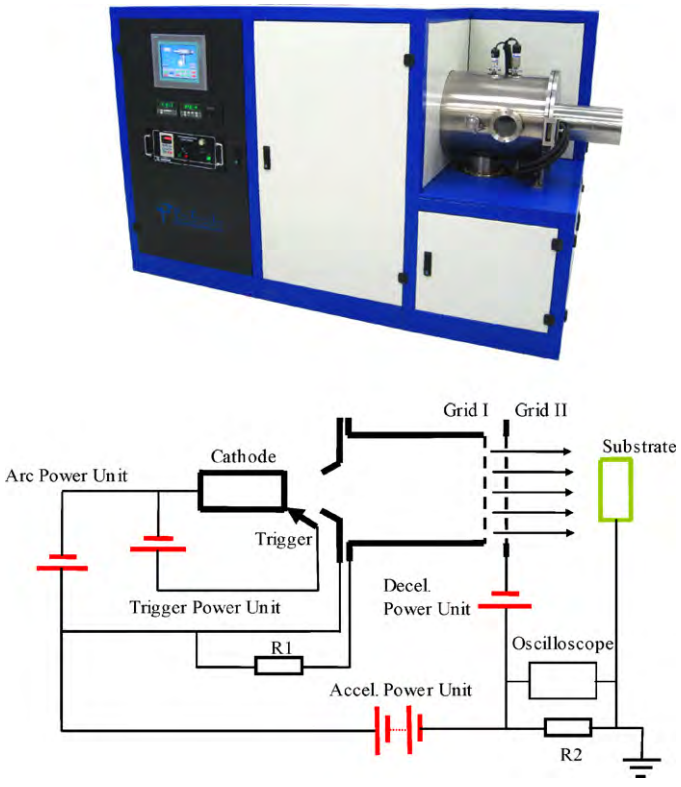

Fig. 1. Photo and schematic diagram of the HEMII-80 high-energy metal ion implanter in the Plasma Laboratory of City University of Hong Kong.

where k is the empirical coefficient usually between 0.30 and 0.35, I_m is the average current, τ is the pulse width being 1 ms, n is the number of pulses, e is the electron charge, S is the ion beam area, and $\bar{n}_0$ is the average charge state number which is +1 for carbon [30]. The calculated ion implantation fluences are about 6×10^{16} ions cm^{-2}, 1.2×10^{17} ions cm^{-2}, 2.4×10^{17} ions cm^{-2}, and 4.8×10^{17} ions cm^{-2} for samples C – 0.25 h, C – 0.5 h, C – 1 h, and C – 2 h, respectively.

Elemental depth profiles and chemical states were determined by X-ray photoelectron spectroscopy (XPS) using a Kratos AXIS Ultra equipped with a monochromatic Al Kα radiation source operated at a constant pass energy of 11.75 eV, take-off angle of 45°, and a step size of 0.25 eV. The Fe, Cr, Ni, Mo, O and C depth profiles were obtained by 3 kV Ar sputtering of a 3 mm × 3 mm area to ensure that artifacts from the crater walls and induced roughness were minimized. The cross-sectional microstructure of the implanted SS316L samples was examined by transmission electron microscopy (TEM, FEI TECHAI G^2 F20 operated at 200 kV).

2.2. Ex situ evaluation

The *ex situ* evaluation of the bipolar plate materials included ICR measurement, electrochemical tests, and contact angle determination. The ICR was determined from structures consisting of two pieces of conductive carbon paper (Toray TGP-H-090) sandwiched between the sample and two copper plates. A constant current of 0.1 A was applied through the two copper plates and the voltage was monitored as a function of steadily increasing compaction force. The ICR values reported here had been background subtracted.

The electrochemical behavior was examined by potentiodynamic and potentiostatic tests. The amounts of corroded metallic ions during the potentiostatic test were determined by inductively coupled plasma optical emission spectrometry (ICP-OES). The electrochemical tests were carried out on a Zahner Zennium Electrochemical Workstation and the electrolyte composition was 0.5 M H_2SO_4 + 2 ppm HF at 80 °C to simulate the aggressive PEMFC environment. The solution was purged with either air or hydrogen to simulate the cathode or anode environment prior to and during the electrochemical test. Potentiodynamic polarization was performed at a scanning rate of 1 mV s^{-1}. To investigate the stability of the samples in the aggressive PEMFC environment, the potentiostatic test was carried out for 10 h at a potential of 0.6 V vs. SCE while being purged with air and −0.1 V vs. SCE being purged with H_2 to simulate the cathode and anode environments in the PEMFC, respectively. After the potentiostatic test, 100 mL of the solution were collected and analyzed by ICP-OES to determine the concentration of Fe, Cr, Ni, and Mo in the solution.

2.3. In situ evaluation: single cell test

In the *in situ* analysis, single cell tests were conducted to investigate the improvement of carbon ion implantation in power density. According to the ICR and corrosion resistance results, sample C – 2 h (0.1 mm thick SS implanted with C for 2 h) was selected for the test and a single cell with unimplanted SS bipolar plates was also assembled and tested for comparison. The performance of the single cell was evaluated by the *I–V* characteristics determined using the NBT-100W fuel cell test system. The experiments were performed under the scanning current mode and the results were recorded after 2 h of stable operation. A commercial MEA with 0.5 mg cm^{-2} platinum and an active electrode area of 40 cm^2 was adopted on both the anode and cathode sides. Aluminum plates of 15 mm thick were used as the end plates and 2 mm thick brass plates were used to collect the current. The bipolar plates, MEAs, silicon seals, and current collectors were clamped between the two end plates by eight

Table 2
Main operating conditions in the single cell test.

Parameter	Cathode side	Anode side
Active area	40 cm^2	40 cm^2
Reactant flow rate	1000 SCCM (O_2)	1200 SCCM (H_2)
Back pressure	50 kPa	30 kPa
Reactant gas pressure	0.3 MPa	0.3 MPa
Humidification	30%	30%
Cell temperature	50 °C	50 °C
Reactant temperature	60 °C	60 °C

M4 screw joints at a torque of about 6 Nm. The main operating conditions are listed in Table 2.

3. Results and discussion

3.1. XPS and TEM

The elemental depth profile of sample C – 1 h as well as Fe, Cr and Ni XPS spectra are depicted in Fig. 2. As shown in Fig. 2(a), the carbon implanted layer is about 240 nm thick and the carbon depth profile exhibits a Gaussian like distribution with a peak atomic fraction of about 40%. The carbon concentration near the surface is also about 25%, further indicating that ion implantation circumvents thermodynamic constraints such as solubility and phase diagrams [18]. The evolution of the Fe, Cr, and Ni XPS spectra with depths is displayed in Fig. 2(b), (c), and (d), respectively. Fe near the surface exists in both the metallic and oxidized states and at a depth of 1 nm, metallic iron begins to dominant. In the near surface, chromium has mainly the trivalent oxidized state and exists in both the metallic and oxide states at a depth of 1 nm. After sputtering to a depth of 2 nm, chromium changes from the metallic and oxide mixed states to metallic state, indicating the border between the passive film and substrate. Ni exists mainly in the metallic state throughout the entire depth [31].

Fig. 3 depicts the TEM cross-sectional micrographs of the SS316L samples implanted with different fluences. As observed from samples C – 0.25 h (6×10^{16} ions cm^{-2}) and C – 0.5 h (1.2×10^{17} ions cm^{-2}), an amorphous layer with an approximate thickness of 53 nm and 60 nm, respectively, is formed on the surface and there is a zone with fine grains zone underneath the amorphous layer. Formation of the amorphous layer in conjunction with the fine-grain zone significantly reduces the adverse effect of the heterogeneous surface of SS316L and improves the corrosion resistance. Fig. 3(c) and (d) shows the cross-sectional microstructure of samples C – 1 h and C – 2 h. There is a circular nanophase with a diameter of about 10 nm precipitated from original amorphous layer and the distance from the surface to the end of amorphous

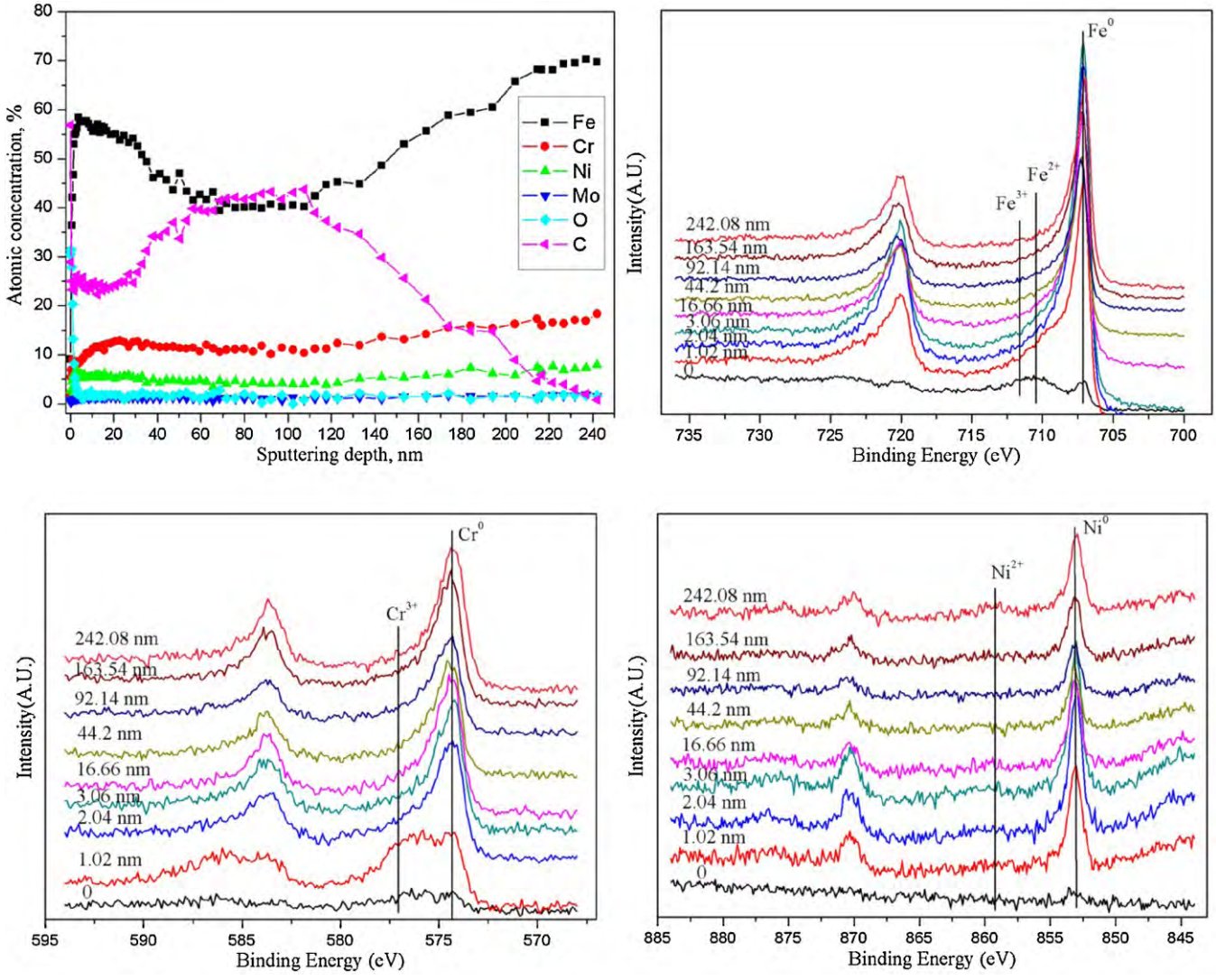

Fig. 2. XPS depth profiles determined from (a) C – 1 h sample and XPS spectra as a function of sputtering depths for (b) Fe, (c) Cr, and (d) Ni.

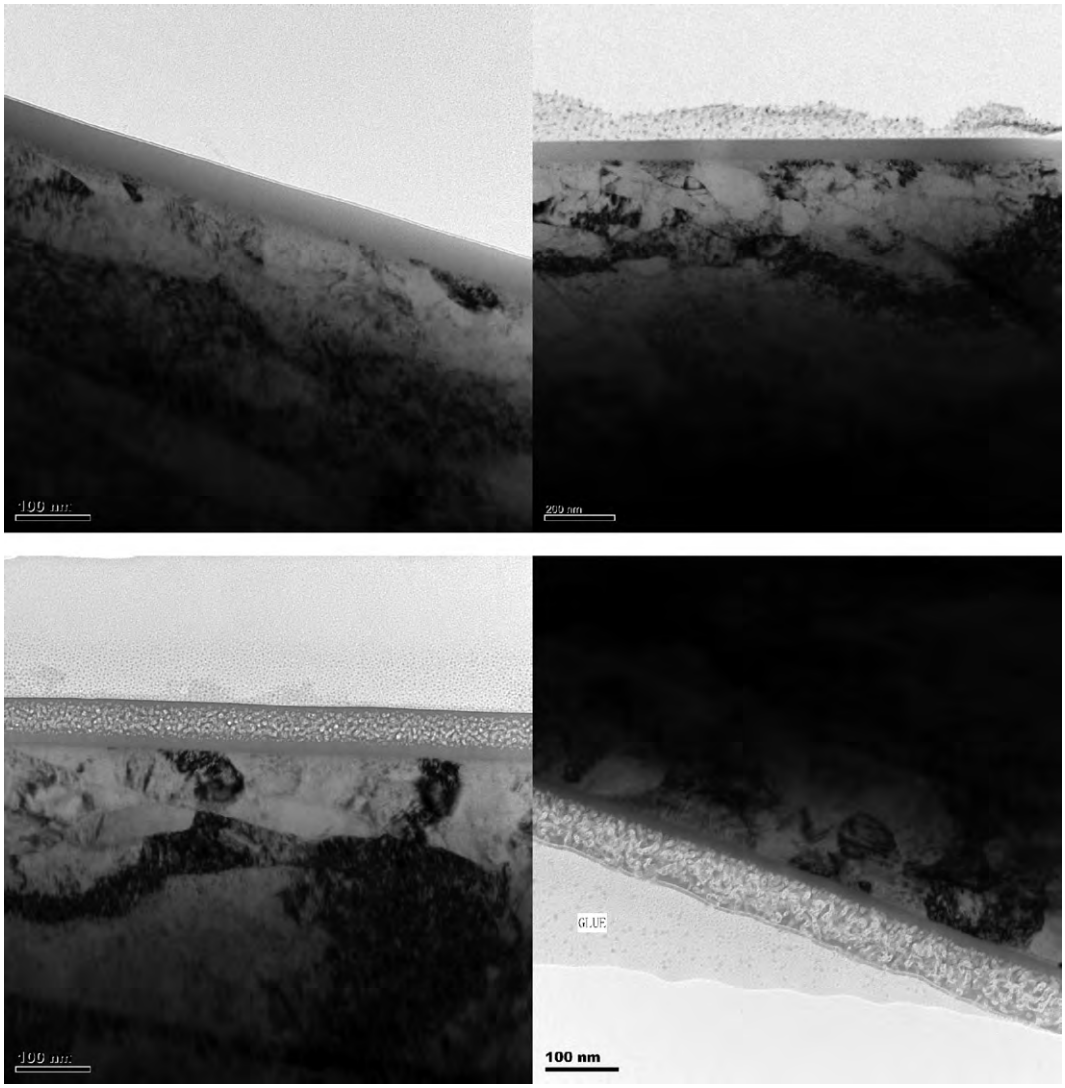

Fig. 3. TEM cross-sectional micrographs of SS316L samples implanted with different C fluences.

layer is 65 nm and 85 nm in samples C – 1 h and C – 2 h, respectively. Underneath the precipitated nanophase zone, an amorphous layer, 16 nm and 18 nm thick, respectively, exists. As shown by the depth profiles, the implanted C is located between 65 nm and 107 nm and it is deeper than the amorphous layer and precipitated nanophase zone. Our results suggest that the amorphous layer and precipitated nanophase zone are formed by implantation-induced damage in lieu of carbon enrichment. The precipitated nanophase is graphite as determined from previous studies involving carbon implanted steel [32–34].

3.2. ICR measurements

The ICR between the SS sample and gas diffusion layer (carbon paper) is a critical factor governing the internal resistance of the PEMFC stack thus affecting the resistance over potential of each single cell [17]. The ICR values as a function of compaction force are presented in Fig. 4. ICR decreases with the compaction force exponentially [35], implying that the compaction force is dominant in the reduction of the ICR in the region of lower compaction force whereas the surface composition is the predominant factor in the region at a larger compaction force. The ICR of SS316L is relatively high at 664.3–255.4 $m\Omega\,cm^2$ at compaction force from

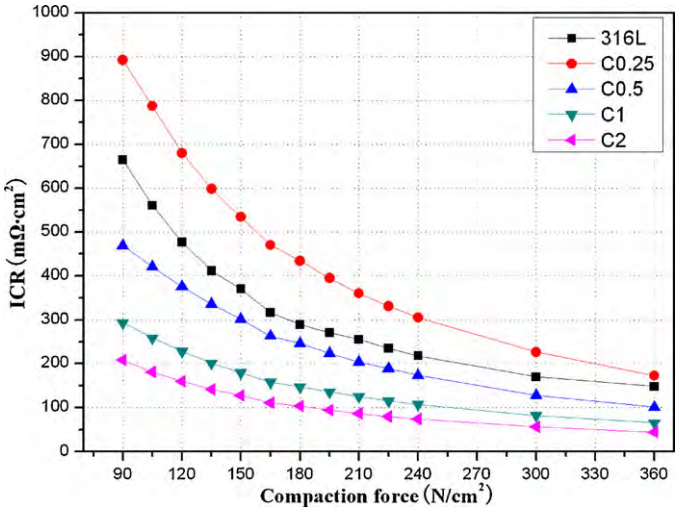

Fig. 4. Variation in ICR values versus compaction force determined from the unimplanted and carbon implanted SS316L.

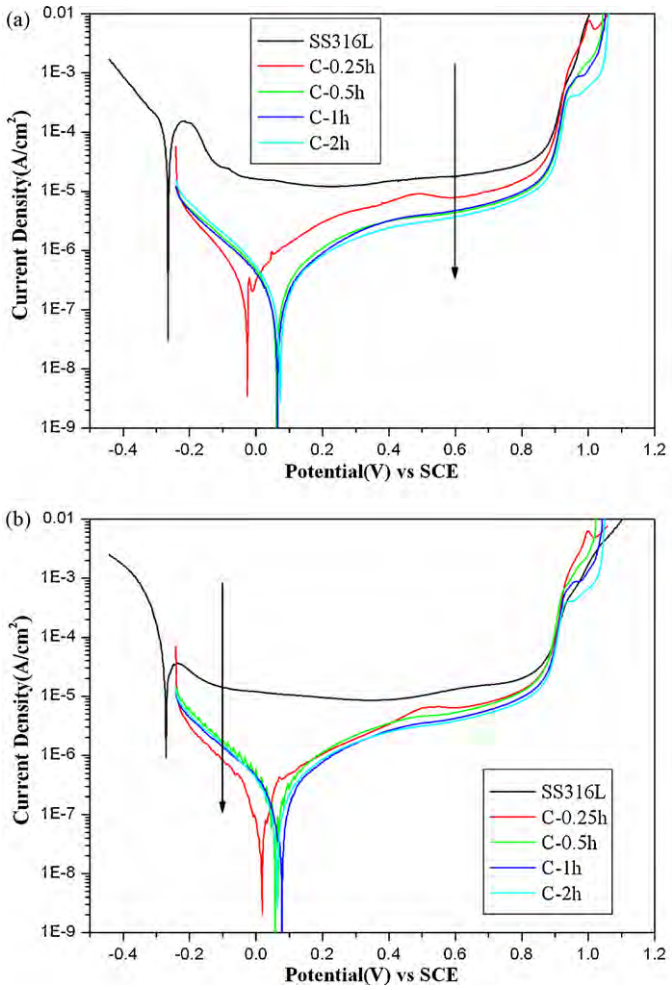

Fig. 5. Potentiodynamic curves obtained from the unimplanted and carbon-implanted SS316L in 0.5 M H_2SO_4 solution with 2 ppm HF at 80 °C: (a) purged with air and (b) purged with H_2.

90 to 210 N cm^{-2} due to the surface passivation layer acting as a semiconductor [36,37]. In the carbon-implanted SS samples, the ICR decreases with increasing ion implantation fluence. Sample C – 0.25 h shows the highest ICR value of 892.3–360.5 mΩ cm^2 at 90–210 N cm^{-2}, which is even higher than that of SS316L. On the other hand, the ICR of sample C – 2 h is much smaller throughout the applied compaction force range and is 207.5–86.8 mΩ cm^2 at 90–210 N cm^{-2}. The actual ICR is mainly influenced by two factors: the contact area between the sample and carbon paper as well as the conductivity of the sample surface. Since the contact area in this study is the same, the difference in the ICR is caused by the latter factor. The surface conductivity is further affected by the surface composition and microstructure. As shown by the cross-sectional microstructure in Fig. 3, the amorphous layer formed by irradiation damage affects the surface conductivity negatively and so the ICR of sample C – 0.25 h increases. As the implantation fluence increases, the carbon concentration increases and chromium and graphite nanophases are precipitated in the surface, both of which are beneficial to the surface conductivity.

3.3. Electrochemical tests and ICP results

The potentiodynamic polarization behavior in 0.5 M H_2SO_4 + 2 ppm HF solution at 80 °C shown in Fig. 5(a) shows the potentiodynamic curves in the simulated PEMFC cathode environment. The corrosion potential of SS316L is −265 mV whereas that of the carbon implanted SS316L is nobler. The corrosion potential of sample C – 0.25 h is −26 mV and that of samples C – 0.5 h, C – 1 h, and C – 2 h is about 65 mV. Thermodynamically, a higher corrosion potential means higher chemical inertness and less corrosion tendency. The bare SS316L exhibits a typical polarization curve of austenitic stainless steel including three regions, namely the active region, passive region, and transpassive region. A very high peak passivating current of about 150 μA cm^{-2} can be observed due to active dissolution and oxidation of the metal. The passivation current density of SS316L is higher at 17.9 μA cm^{-2}. In contrast, the passivation current density after carbon ion implantation is significantly reduced to about 3–4 μA cm^{-2}. The smaller anodic current density usually implies better durability and smaller corrosion rate. Fig. 5(b) displays the potentiodynamic polarization curves in the simulated PEMFC anode environment. Compared to the unimplanted SS316L, the corrosion potential of the carbon-implanted SS316L shifts positively reaching about 50 mV. This is more positive than the operating potential in the PEMFC anode environment. Similar to the potentiodynamic behavior in the cathode environment, the passivation current density is also reduced after carbon ion implantation.

The bipolar plate under the real PEMFC working conditions undergoes corrosion at an applied potential (cathode 0.6 V vs. SCE; anode −0.1 V vs. SCE) which is different from the free corrosion potential. Therefore, the potentiostatic test is conducted to benchmark the corrosion resistance of SS316L in the aggressive PEMFC environment. Fig. 6(a) shows the potentiostatic curves at 0.6 V in the simulated cathode environment. The current density decreases rapidly in the beginning and then gradually stabilizes at about 1.3 μA cm^{-2}. For the carbon implanted SS316L, the current density decreases with increasing ion implantation fluence, being 1.2 μA cm^{-2}, 0.9 μA cm^{-2}, 0.5 μA cm^{-2} and 0.4 μA cm^{-2} for samples C – 0.25 h, C – 0.5 h, C – 1 h and C – 2 h, respectively. Fig. 6(b) presents the potentiostatic curves at −0.1 V in the anode environment. The current density of the unimplanted and carbon implanted SS316L exhibits a totally different behavior. The current density of SS316L decays dramatically, undergoes a positive–negative switch at 2 h, and then maintains at a negative level of about −0.18 μA cm^{-2}. The current density of carbon-implanted samples starts from a lower position, increases dramatically, and then reaches a relatively low level. The different polarization behavior between the unimplanted and carbon implanted SS316L is due to the different corrosion potentials. The corrosion potential of SS316L is lower compared to the applied potential of −0.1 V whereas those of the carbon-implanted samples are higher.

The metal ions leached to the solution due to corrosion are very important in gauging the performance of the bipolar plate materials and a post corrosion analysis is performed. The dissolved metal ions are determined by ICP and the results are summarized in Table 3. It is apparent that the Fe concentration is the highest in all cases due to selective dissolution. The total metal ion concentrations leached from the uncoated SS316L are 9.27 ppm and 7.94 ppm after the potentiostatic test in the simulated PEMFC cathode and anode environments, respectively. In the cathode environment, the metallic ion concentrations leached from the carbon implanted SS316L are greatly reduced. The metallic concentrations decrease as ion implantation fluences increase, reaching a minimum total ion concentration of 0.52 ppm for sample C – 2 h. In contrast, the improvement in the anode environment is not so apparent.

3.4. Single cell test

The initial performance of the single cell assembled with the unimplanted and carbon implanted SS bipolar plate is shown in Fig. 7. The single cell assembled with the carbon implanted SS bipolar plates shows significantly better performance than that

Table 3
Fe, Cr, Ni, and Mo ion concentrations leached from the unimplanted and C-implanted samples after 10 h potentiostatic test.

Sample	Ion concentration in PEMFC cathode environment after 10 h (ppm)					Ion concentration in PEMFC anode environment after 10 h (ppm)				
	Fe	Cr	Ni	Mo	Total	Fe	Cr	Ni	Mo	Total
SS316L	7.62	0.88	0.69	0.08	9.27	6.28	0.90	0.61	0.15	7.94
C15 min	1.00	0.04	0.04	0.01	1.09	2.66	0.05	0.09	0.01	2.81
C0.5 h	0.91	0.02	0.02	–	0.95	2.99	0.03	0.06	–	3.08
C1 h	1.20	0.04	0.05	–	1.29	4.53	0.05	0.08	–	4.66
C2 h	0.47	0.03	0.02	–	0.52	5.70	0.03	0.10	–	5.83

with unimplanted SS bipolar plates. The open circuit voltage (OCV) of the single cell with the C-implanted bipolar plates is almost the same as that of the unimplanted SS bipolar plates, being 979.6 mV and 976.7 mV, respectively. The peak power density of the single cell assembled with the unimplanted SS bipolar plates is 566.5 mW cm^{-2} at a current density of 1351.7 mA cm^{-2} and the power density at 0.6 V is 299.7 mW cm^{-2}. As for the carbon implanted bipolar plates, the peak power density is 840.0 mW cm^{-2} at a current density of 2128.9 mA cm^{-2}, while the power density is 581.1 mW cm^{-2} at 0.6 V. It is noted that the power density at 0.6 V increases almost by a factor of 2 after carbon ion implantation. Since the assembling and test conditions are the same, the performance of the single cell is affected by resistance over-potential. As the sweeping current density increases, the output voltage of the single cell

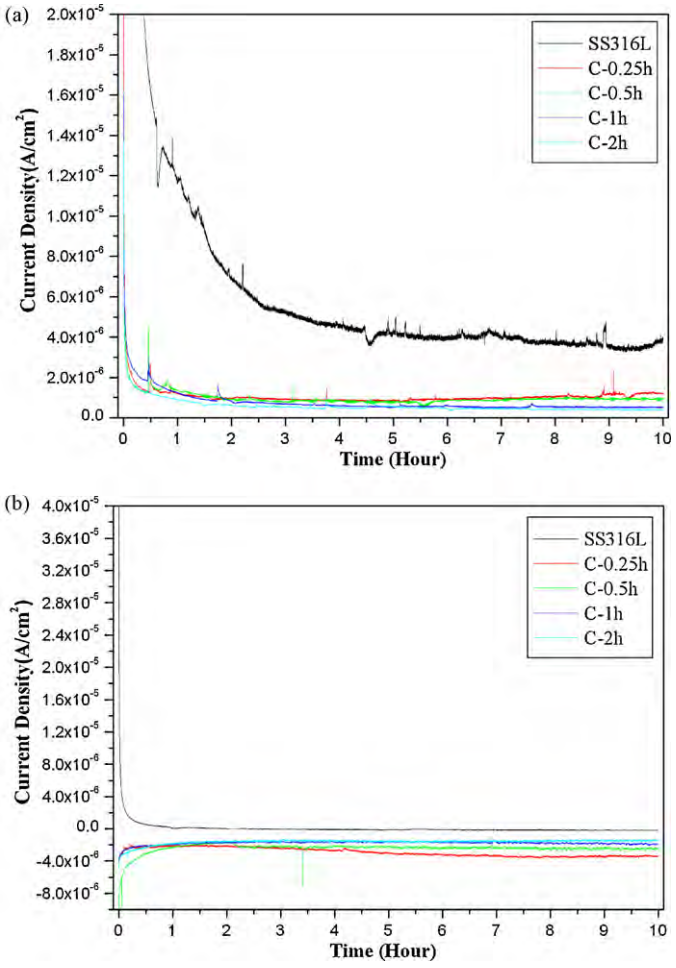

Fig. 6. Potentiostatic curves of the unimplanted and carbon-implanted SS316L in the (a) simulated cathode (0.6 V vs. SCE purged with air) and (b) anode environment (−0.1 V vs. SCE purged with H_2).

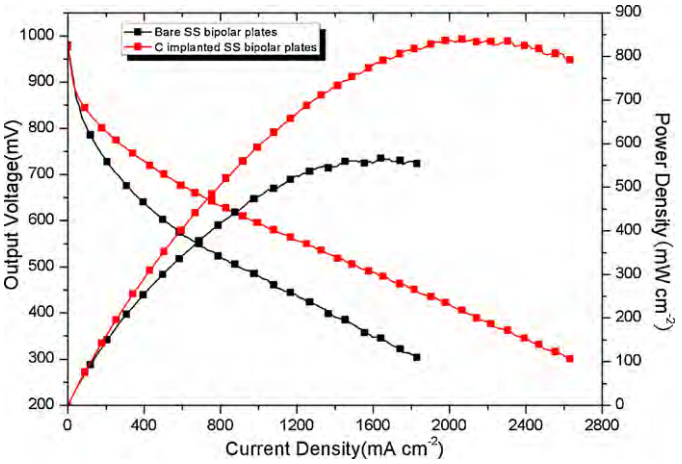

Fig. 7. Initial performance of the single cells assembled with the unimplanted and carbon-implanted SS bipolar plates.

with the unimplanted SS bipolar plates decreases faster than that measured from the C implanted SS bipolar plates due to a much higher ICR as illustrated in Fig. 4. The single cell test result reveals that the formation of the carbon-enriched nanophase precipitated zone greatly enhances the surface conductivity of the SS bipolar plates consequently boosting the single cell performance.

4. Conclusion

Carbon ion implantation is employed to improve the surface conductivity and corrosion resistance of stainless steel bipolar plate materials. The performance is evaluated by various *ex situ* and *in situ* methods. An amorphous layer is formed when the ion implant fluence is small and at higher fluences, a precipitated nanophase zone and amorphous layer can be observed. The ICR decreases with increases of ion implantation fluence and the smallest value is observed from sample C – 2 h (207.5–86.8 mΩ cm^2 at compaction force of 90–210 N cm^{-2}) due to carbon and the precipitate nanophase. The potentiodynamic test, potentiostatic test, and ICP measurement reveal that the corrosion resistance is significantly improved after carbon ion implantation. In particular, the current densities under the cathode operation potential diminish from 17.9 μA cm^{-2} to 3–4 μA cm^{-2}. The corrosion potentials shift positively from about −0.3 V to 0.05 V in the simulated anode environment and are nobler than the anode operating potential. The potentiostatic and ICP results show that the carbon-implanted SS316L is stable and has better corrosion resistance, especially in the simulated cathode environment. The *in situ* single cell tests show that the peak power density of single cell with the ion-implanted bipolar plates increases from 566.5 mW cm^{-2} to about 840.0 mW cm^{-2} and the power density at 0.6 V increases by almost a factor of 2 compared to the single cell assembled with the unimplanted SS bipolar plates.

Acknowledgements

Financial support was provided by National Natural Science Foundation of China under contract number 50820125506 and No. 50971091, National High Technology Research and Development Program 863 under contract number 2009AA05Z120, the Ministry of Science and Technology of the People's Republic of China (Grant No. 2009DFB50350), and Hong Kong Research Grants Council (RGC), General Research Funds (GRF) No. CityU 112510. The authors also thank Linfa Peng, Peiyun Yi, and Diankai Qiu in the School of Mechanical Engineering, SJTU for their assistance in the ICR and single cell measurements.

References

[1] X. Li, I. Sabir, Int. J. Hydrogen Energy 30 (2005) 359–371.
[2] Y. Wang, K.S. Chen, J. Mishler, S.C. Cho, X.C. Adroher, Appl. Energy 88 (2011) 981–1007.
[3] A. Hermann, T. Chaudhuri, P. Spagnol, Int. J. Hydrogen Energy 30 (2005) 1297–1302.
[4] J.F. Wu, X.Z. Yuan, J.J. Martin, H.J. Wang, J.J. Zhang, J. Shen, S.H. Wu, W. Merida, J. Power Sources 184 (1) (2008) 104–119.
[5] H. Wang, J.A. Turner, Fuel Cells 10 (2010) 510–519.
[6] I. Bar-On, R. Kirchaina, R. Roth, J. Power Sources 109 (2002) 71–75.
[7] B.C.H. Steele, A. Heinzel, Nature 414 (2001) 345–352.
[8] V. Mehta, J.S. Cooper, J. Power Sources 14 (1) (2003) 32–53.
[9] A. Kumar, M. Ricketts, S. Hirano, J. Power Sources 195 (2010) 1401–1407.
[10] J. Wind, R. Spah, W. Kaiser, G. Bohm, J. Power Sources 105 (2002) 256–260.
[11] R.C. Makkus, A.H.H. Janssen, F.A. de Bruijn, R.K.A.M. Mallant, J. Power Sources 86 (2000) 274–282.
[12] D.P. Davies, P.L. Adcock, M. Turpin, S.J. Rowen, J. Power Sources 86 (2000) 237–242.
[13] E.A. Cho, U.S. Jeon, S.A. Hong, I.H. Oh, S.G. Kang, J. Power Sources 142 (2005) 177–183.
[14] H. Tawfik, Y. Hung, D. Mahajan, J. Power Sources 163 (2007) 755–767.
[15] K. Feng, Y. Shen, J. Mai, D. Liu, X. Cai, J. Power Sources 182 (2008) 145–152.
[16] M.P. Brady, K. Wersbrod, I. Paulauskas, R.A. Buchanan, K.L. More, H. Wang, et al., Scripta Mater. 50 (2004) 1017–1022.
[17] P. Yi, L. Peng, L. Feng, P. Gan, X. Lai, J. Power Sources 195 (2010) 7061–7066.
[18] R.A. Antunes, M.C.L. Oliveira, G. Ett, V. Ett, Int. J. Hydrogen Energy 35 (2010) 3632.
[19] M. Xu, L.H. Li, Y.M. Liu, X. Cai, Q.L. Chen, P.K. Chu, Mater. Sci. Eng. A 425 (2006) 1.
[20] X.Y. Liu, P.K. Chu, C.X. Ding, Mater. Sci. Eng. R: Rep. 47 (2004) 49.
[21] A. Anders, Surf. Coat. Technol. 183 (2004) 301.
[22] P.K. Chu, S. Qin, C. Chan, N.W. Cheung, L.A. Larson, Mater. Sci. Eng. R: Rep. 17 (1996) 207.
[23] N. Theodoropoulou, A.F. Hebard, S.N.G. Chu, M.E. Overberg, C.R. Abernathy, S.J. Pearton, R.G. Wilson, J.M. Zavada, J. Appl. Phys. 91 (2002) 7499.
[24] T. Fukutsuka, T. Yamaguchi, S.I. Miyano, Y. Matsuo, Y. Sugie, Z. Ogumi, J. Power Sources 174 (2007) 199–205.
[25] Y. Show, M. Miki, T. Nakamura, Diam. Relat. Mater. 16 (2007) 1159–1161.
[26] C.Y. Chung, S.K. Chen, P.J. Chiu, M.H. Chang, T.T. Hung, T.H. Ko, J. Power Sources 176 (2008) 276–281.
[27] Y. Wang, L. Pham, G.P.S.D. Vasconcellos, M. Madou, J. Power Sources 195 (2010) 4796–4803.
[28] V.V. Nikam, R.G. Reddy, S.R. Collins, P.C. Williams, G.H. Schiroky, G.W. Henrich, Electrochim. Acta 53 (2008) 2743–2750.
[29] M.-U. Kim, D.-H. Kim, S.-H. Han, E. Fleury, H.-K. Seok, P.-R. Cha, Y.-C. Kim, Met. Mater. Int. 17 (2011) 283–289.
[30] G.Y. Yushkov, A. Anders, E.M. Oks, I.G. Brown, J. Appl. Phys. 88 (2000) 5618.
[31] C.O.A. Olsson, D. Landolt, Electrochim. Acta 48 (2003) 1093–1104.
[32] J.L. Viviente, A. Garcia, F. Alonso, I. Braceras, J.I. Onate, Appl. Surf. Sci. 144–145 (1999) 249–254.
[33] R. Sanchez, J.A. Garcia, A. Medrano, M. Rico, R. Martinez, R. Rodriguez, C. Fernandez-Ramos, A. Fernandez, Surf. Coat. Technol. 158–159 (2002) 630–635.
[34] J.L. Viviente, A. Garcia, A. Loinaz, F. Alonso, J.I. Onate, Vacuum 52 (1999) 141–146.
[35] Y. Fu, M. Hou, D. Liang, X. Yan, Y. Fu, Z. Shao, Z. Hou, P. Ming, B. Yi, Carbon 46 (2008) 19.
[36] M.Z. Yang, J.L. Luo, Q. Yang, L.J. Qiao, Z.Q. Qin, P.R. Norton, J. Electrochem. Soc. 146 (1999) 2107.
[37] A.K. Iversen, Corros. Sci. 48 (2006) 1036.